Wave-packet self-imaging and giant recombinations via stable Bloch-Zener oscillations in photonic lattices with local PT symmetry

N. Bender, H. Li, F. M. Ellis, and T. Kottos

Phys. Rev. A **92**, 041803 — Published 12 October 2015

DOI: 10.1103/PhysRevA.92.041803

Wavepacket Self-imaging and Giant Recombinations via Stable Bloch-Zener Oscillations in Photonic Lattices with Local $\mathcal{PT}$-Symmetry

N. Bender, H. Li, F. M. Ellis, T. Kottos
Department of Physics, Wesleyan University, Middletown, CT-06459, USA

We propose a family of *local* $\mathcal{PT}$-symmetric photonic lattices with transverse refraction index gradient ω, where the emergence of *stable* Bloch-Zener oscillations are controlled by the interplay of ω with the degree of non-Hermiticity γ of the lattice. In the exact $\mathcal{PT}$-symmetric phase we identify a condition between ω and γ for which a wavepacket self-imaging together with a cascade of splittings and giant recombinations occurs at various propagation distances. The giant wavepacket recombination is further enhanced by introducing local impurities.

PACS numbers: 42.82.Et, 11.30.Er, 42.25.Bs

Introduction - Non-Hermitian wave physics and specifically its parity-time ($\mathcal{PT}$) symmetric ramifications [1], has attracted a lot of attention in recent years. The main observation was that a non-Hermitian Hamiltonian $\mathcal{H}$ that commutes with the joint $\mathcal{PT}$ -symmetric operator may possess an entirely real spectrum. Specifically it was shown that below a critical value $\gamma_{\mathcal{PT}}$, of the gain/loss parameter γ controlling the non-Hermiticity of $\mathcal{H}$, the spectrum is real and the eigenfunctions of $\mathcal{H}$ are eigenfunctions of the $\mathcal{PT}$-symmetric operator. In the opposite limit the spectrum becomes partially or completely complex while the eigenfunctions cease to be eigenfunctions of the $\mathcal{PT}$ operator. The first domain was coined the exact $\mathcal{PT}$-symmetric phase while the latter was coined the broken $\mathcal{PT}$-symmetric phase. The transition point $\gamma = \gamma_{\mathcal{PT}}$ is characterized by an exceptional point (EP) singularity where both the eigenfunctions and eigenvalues coalesce.

The impact of these ideas is well documented in various physical settings ranging from matter waves [2, 3] and magnonics [4] to optics [5–18], electronics [19] and acoustics [20]. Among the theoretical predictions [13], and subsequent experimental realizations [8], was a new type of Bloch Oscillations which were unstable. They either amplified or attenuated since the propagating constants at these $\mathcal{PT}$-symmetric lattices became immediately complex (the system is at the broken $\mathcal{PT}$-phase) once a transverse refraction index gradient is introduced.

Here we introduce a class of photonic lattices, whose building blocks are $\mathcal{PT}$-symmetric dimers (see Fig. 1a), with a transverse refractive index gradient ω. These lattices respect a *local* $\mathcal{P}_d\mathcal{T}$-symmetry associated with each individual dimer. Despite the lack of global $\mathcal{PT}$-symmetry they have parameter domains for which their eigenvalues are real (i.e. exact $\mathcal{PT}$-phase). In this domain they support a class of *stable* $\mathcal{PT}$-symmetric Bloch-Zener oscillations which, allow for periodic wavepacket self- imaging whenever the choice of the $\omega-\gamma$ parameters imposes a commensurability relation between the period of Zener tunneling and the period of Bloch-Oscillations. These Bloch-Zener oscillations experience a cascade of splittings and giant beam recombinations which are further enhanced in the presence of localized defects.

Theoretical Model– We consider the photonic lattice of Fig. 1a. Each waveguide supports only one propagating mode, while light is transferred between waveguides via evanescent tunneling. The connectivity of the array is such that each amplifying (dissipative) waveguide of a dimer is coupled, with a coupling constant $\frac{A}{2}$, to both of the adjacent dimers' dissipating (amplifying) waveguide. In addition we assume an intra-dimer coupling α [25]. An experimental implementation of the refraction index gradient has been realized in Ref. [21, 22] for 1D structures and for 2D structures in Ref. [23, 24]. The diffraction dynamics of the evolving electric field amplitude $\Psi_n(z) = (a_n(z), b_n(z))^T$ of the n^{th} dimer along the propagation direction z, in the paraxial description, satisfies the following equation

$$\begin{aligned} i\frac{da_n}{dz} + (n\omega - i\gamma)a_n + \alpha b_n + \frac{A}{2}(b_{n-1} + b_{n+1}) = 0 \\ i\frac{db_n}{dz} + (n\omega + i\gamma)b_n + \alpha a_n + \frac{A}{2}(a_{n-1} + a_{n+1}) = 0 \end{aligned} \tag{1}$$

where $a_n(b_n)$ is the field amplitude at the gain (loss) site of the n-th dimer. Although the system described by Eq. (1) does not respect a global $\mathcal{PT}$-symmetry (due to the index gradient), nevertheless there is a *local* $\mathcal{P}_d\mathcal{T}$ symmetry that it is satisfied by each *individual dimer* (i.e. each dimer is $\mathcal{PT}$-symmetric around its axis of symmetry) [26]. A realization of the basic $\mathcal{PT}$-symmetric unit of our structure, i.e. the $\mathcal{PT}$-dimer, (and how to control the gain/loss parameter γ) was demonstrated in [6].

Spectral Analysis– It is instructive to start by studying the dispersion relation of the system in the absence of the transverse index gradient i.e. $\omega = 0$. Using the Fourier transformation $a_n(z) = \frac{1}{\sqrt{2\pi}}\int_{-\pi}^{\pi} \tilde{a}_q(z)e^{iqn}dq$ (similarly for $b_n(z)$) Eq. (1) takes the form:

$$i\frac{d}{dz}\begin{pmatrix} \tilde{a}_q(z) \\ \tilde{b}_q(z) \end{pmatrix} = \begin{pmatrix} i\gamma & -v_q \\ -v_q & -i\gamma \end{pmatrix}\begin{pmatrix} \tilde{a}_q(z) \\ \tilde{b}_q(z) \end{pmatrix} \tag{2}$$

where $v_q = \alpha + A\cos(q)$. The dispersion relation $\mathcal{E}^\sigma(q)$ (longitudinal propagation constants) is obtained by calculating the eigenvalues of the 2×2 matrix in Eq. (2):

$$\mathcal{E}^\sigma(q) = \sigma\sqrt{(\alpha + A\cos[q])^2 - \gamma^2} \tag{3}$$

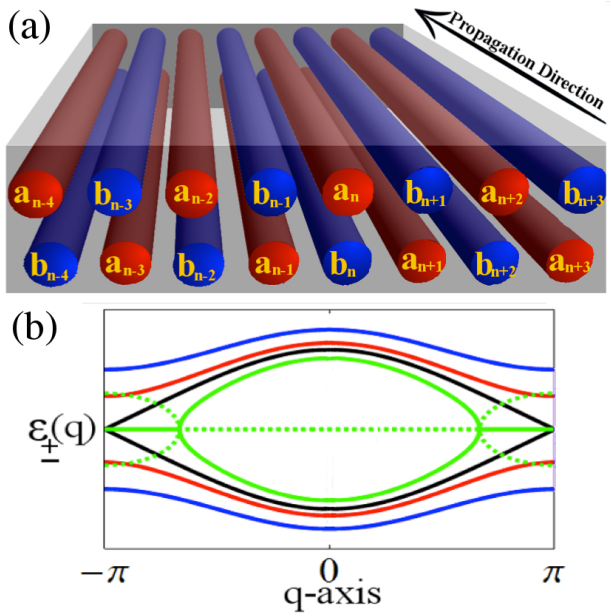

FIG. 1: (Color online) (a) The photonic lattice (for $\omega = 0$) with $\mathcal{P}_d\mathcal{T}$-symmetry [26]. Red (blue) waveguides indicate waveguides with amplification (attenuation) [25]. (b) The associated dispersion relation for $\gamma = 0$ (blue), $0 \leq \gamma \leq \gamma_{\mathcal{PT}}$ (red), $\gamma = \gamma_{\mathcal{PT}}$(black), and the solid/dashed green lines are the real/imaginary part for $\gamma > \gamma_{\mathcal{PT}}$.

where $q \in (-\pi, \pi]$ and $\sigma = \pm$ indicates the upper/lower band. For $\gamma = 0$ the minimal spacing between the two bands $\delta = 2(\alpha - A)$ occurs at $q = \pm\pi$. As γ increases the minimal band separation shrinks until the edges touch at $\gamma \to \gamma^{\mathcal{PT}} = \alpha - A$ where an EP degeneracy occurs (see Fig. 1b). For $\gamma > \gamma_{\mathcal{PT}}$ we enter the broken $\mathcal{PT}$-symmetric phase and the eigenvalues appear in complex conjugate pairs. Below we will focus our analysis on the parameter domain for which the spectrum is real (exact $\mathcal{PT}$-symmetric phase). In this domain, the eigenvectors $|\sigma\rangle$ of the 2×2 matrix of Eq. (2) take the form

$$|\sigma\rangle = \frac{\sqrt{-\sigma}}{\sqrt{2\cos\theta}} \begin{bmatrix} e^{-i\sigma\theta/2} \\ -\sigma e^{i\sigma\theta/2} \end{bmatrix}; \; \theta = \arcsin\left(-\frac{\gamma}{v_q}\right) \qquad (4)$$

and they are also eigenvectors of the $\mathcal{PT}$-operator [1].

When $\omega \neq 0$ the two bands are replaced by two interleaving Wannier-Stark ladders $\mathcal{E}_n^{\pm} = \mathcal{E}_0^{\pm} + n\omega$ where $n = 0, \pm 1, \cdots$. The offsets $\mathcal{E}_0^{\pm}$ determine the relative energy distance between the two ladders and can be evaluated numerically from a direct diagonalization of the effective Hamiltonian H that describes the paraxial propagation of our system Eq. (1). In contrast to the $\omega = 0$ case, the system possess multiple exceptional points.

Let us look at the case $A = 0$. In this case the longitudinal propagation constants $\mathcal{E}_n^{\pm}$ are organized in doublets associated with the n^{th} isolated dimer:

$$\mathcal{E}_n^{\pm} = \mathcal{E}_0^{\pm} + n\omega; \quad \mathcal{E}_0^{\pm} = \pm\sqrt{\alpha^2 - \gamma^2} \qquad (5)$$

For $\omega > 2\alpha$ the spectrum is non-degenerate for any value of $\gamma \neq \alpha$ (for $\gamma = \alpha$ we have multiple EP degeneracies). However for $\omega = 2\alpha$ we have a degeneracy at $\gamma = 0$, where $\mathcal{E}_n^{\pm} = \mathcal{E}_{n\pm1}^{\mp}$. For $\omega = \alpha$ another (simple) degeneracy develops at $\gamma = 0$ where now $\mathcal{E}_n^{\pm} = \mathcal{E}_{n\pm2}^{\mp}$. At the same time the previous degeneracy at $\gamma = 0$ for $\omega = 2\alpha$, "evolves" towards $\gamma = \alpha\frac{\sqrt{3}}{2}$. It is straightforward to show that for $\omega_m = \frac{2\alpha}{m}$, where $m = 1, 2, 3, ...$, degeneracies with more remote dimers occur at $\gamma = 0$ while the previous ones evolve towards larger values of γ. The index m, defining the number of degeneracies for $A = 0$, will be used below in order to delineate the $\omega - A$ parameter space of our system, Eq. (1), into broken $\mathcal{PT}$- symmetry (i.e. unstable) regions occurring as γ increases.

In Fig. 2a, we present a density plot for $\gamma_{\mathcal{PT}}^{\min}$, associated with the first EP, versus ω and A. The purple horizontal lines indicate the ω_m-values discussed previously. For each such domain, we plot in Figs. 2b- 2d, a typical spectral behavior (for fixed A, ω) of the eigenenergies of the system Eq. (1) versus γ. Thus the number of instability regions is described approximately by the index m. Although this description is good for $A \ll \alpha$, for large A-values a more refined analysis of the number of instability regions is needed.

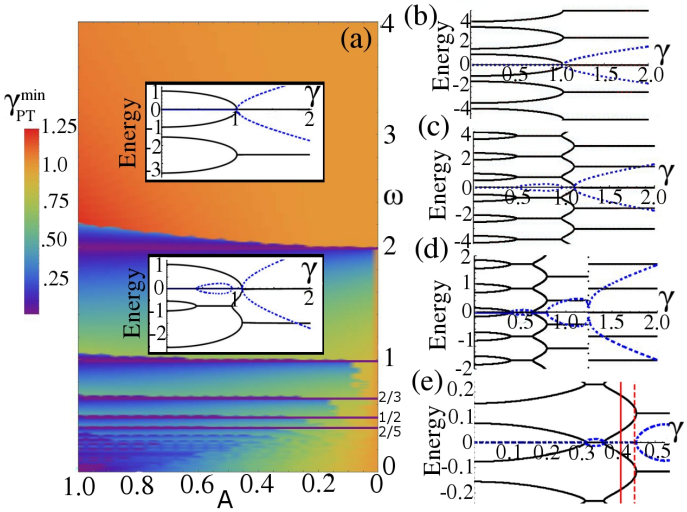

FIG. 2: (Color online) Numerical results for: (a) the first EP of the system for $\alpha = 1$, versus ω and A; (b-d) The real (black) and imaginary (blue) spectra in domains 1, 2, 3 for $A = 0.5$ and $\alpha = 1$. In (b) $\omega = 2.5$, in (c) $\omega = 1.5$ and in (d) $\omega = 0.85$. (e) shows the spectrum for $A = 0.6, \omega = 0.231$ associated with the parameters used in Fig. 3. The perpendicular solid (dashed) lines indicate the values of $\gamma = 0.405(\gamma = 0.443)$ associated with Fig. 3(b,c). The sub-figures in (a) are plots of Eq. (5, 6) respectively for the same parameters as (b) and (c). The purple lines indicate the ω_m-values separating domains with different number of instability regions (see text).

The domain $m = 1$ (one instability region, see Fig. 2b, can be understood within the framework of a single dimer, see Eq. (5). The latter is also plotted at the inset in Fig. 2a. Domain $m = 2$, can be analyzed using two

coupled dimers subjected to a gradient ω:

$$H = -\begin{bmatrix} \bar{n}\omega - i\gamma & \alpha & 0 & \frac{A}{2} \\ \alpha & \bar{n}\omega + i\gamma & \frac{A}{2} & 0 \\ 0 & \frac{A}{2} & (\bar{n}-1)\omega - i\gamma & \alpha \\ \frac{A}{2} & 0 & \alpha & (\bar{n}-1)\omega + i\gamma \end{bmatrix}$$

Direct diagonalization of the above Hamiltonian gives:

$$\mathcal{E}_n = \mathcal{E}_0^{\pm} + n\omega; \quad \mathcal{E}_0^{\pm} = \pm\sqrt{X \pm Y} + \frac{1}{2}\omega \tag{6}$$

where $X \equiv (\frac{A}{2})^2 + \alpha^2 - \gamma^2 + (\frac{\omega}{2})^2$, and $Y \equiv \sqrt{A^2\alpha^2 + (\alpha^2 - \gamma^2)\omega^2}$. Eq. (6) is plotted in the inset of Fig. 2a and it describes qualitatively the features (i.e. two instability domains) shown in Fig. 2c associated with the system Eq. (1). Other domains $m = 3, 4, \cdots$ can be explained by analyzing a system of three, four, etc. coupled dimers. Below we will concentrate only in the parameter space for which the system is in the exact $\mathcal{PT}$-symmetric phase (stable domains) [27].

Dynamics– To study the dynamics, we have numerically simulated the propagation of a broad Gaussian beam for different values of $\gamma \leq \gamma_{\mathcal{PT}}$. We have assumed a normal incident, so that at the input plane $z = 0$ the beam has excited mainly the first band in a spectral interval around $q_0 \approx 0$. We first consider the case of $\gamma = 0$ where the band-gap $\delta = 2(\alpha - A)$ is large enough to allow us to neglect Zener tunneling (ZT). According to the acceleration theorem, the transverse propagation constant q increases up to $\pm\pi$ where the wavelength satisfies the Bragg condition associated with the underlying periodic potential. The wave is then Bragg reflected at propagation distance $z = \pi/\omega$ and travels in the opposite transverse direction toward lower index sites where it experiences a total internal reflection. The process repeats itself leading to a periodic motion which can be considered the optical analogue of Bloch Oscillations. The oscillation period can be easily estimated using the above considerations and it is $z_B = 2\pi/\omega$. The above qualitative picture is nicely reproduced in Fig. 3a for $\gamma = 0$ and $\omega = 0.231$.

As γ increases the band-gap δ becomes smaller and ZT between the two bands at $q = \pm\pi$ is not negligible any more. The associated spreading scenario is depicted in Figs. 3b,c for $\omega = 0.231$ and two different values of the gain/loss parameter $\gamma = 0.405$ and 0.443. In this case the beam will experience a ZT at distances $z_Z^{(n)} = (2n+1)\pi/\omega$, where $n = 0, 1, \cdots$. Let us discuss in more detail the first ZT event at $z_Z^{(0)} = \pi/\omega$. For distances $z < z_Z^{(0)}$ the beam is mainly trapped in the lower band and propagates along the direction of the local gradient $\partial\mathcal{E}^-/\partial q$. At $z_Z^{(0)}$, due to the tunneling, the beam splits into two beams one characterized by the lower band and the other by the upper band. While the beam associated with the lower band reverses direction via Bragg reflection, the beam associated with the upper band follows a parallel trajectory with $\partial\mathcal{E}^+/\partial q$. These two beams will again change direction due to total internal and Bragg reflections respectively. They recombine at the second tunneling point at distance $z_Z^{(1)} = 3\pi/\omega$. The recombination process is more complicated as now both occupied bands experience coherent interference. We have found that at distances $z_R = z_Z^{(2)}$ (marked by the third green line in Fig. 3c) these recombinations can lead to a giant power focus (the total power is plotted with red line in the z-axis of all upper subfigures of Fig. 3). The superposition of ZT with Bloch Oscillations can, in general, result in an asynchronous [28] process which destroys exact revivals of the initial packet. Nevertheless we find that wavepacket self-imaging is achieved for some values of $\omega - \gamma$. This is the case in Fig. 3c (distance $z_{\rm SI}$ indicated by orange line) as opposed to the results shown in Fig. 3b where the self-imaging is not observed.

The dynamics is best analyzed in terms of the Floquet-Bloch (FB) eigenvectors of the effective non-Hermitian Hamiltonian H that describes our system Eq. (1). In Dirac's notation, the FB modes associated with the propagation constant (eigenstate of H) $\mathcal{E}_n^\sigma$ is indicated as $|\mathcal{E}_n^\sigma\rangle$. They constitute a bi-orthogonal basis and satisfy the relations $\langle\mathcal{E}_n^{\sigma *} \left| \mathcal{E}_m^{\sigma'} \right\rangle = \delta_{n,m}\delta_{\sigma,\sigma'}$; $\sum_{\sigma=\pm}\sum_{n=-\infty}^{\infty} |\mathcal{E}_n^\sigma\rangle \langle\mathcal{E}_n^{\sigma *}| = \mathbf{1}$, which are dictated by the symmetric nature of H ($*$ denotes complex conjugation). It is easy to show that the FB modes, in the position representation satisfy the periodicity relation $\langle\mu, l+k\,|\,\mathcal{E}_{n+k}^\sigma\rangle = \langle\mu, l\,|\mathcal{E}_n^\sigma\rangle$; $\{|\mu, l\rangle\}$ is an orthonormal basis defined by two indexes (μ, l) with the first index representing the 'gain' ($\mu = 1$) or 'loss' ($\mu = 2$) waveguide while the second one denoting the label for the dimer.

Next, we expand the initial preparation $|\Psi(0)\rangle$ in the FB basis. We have $|\Psi(0)\rangle = \sum_{\sigma=\pm}\sum_{n=-\infty}^{\infty} c_n^\sigma |\mathcal{E}_n^\sigma\rangle$ where $c_n^\sigma \equiv \langle\mathcal{E}_n^{\sigma *}|\,\Psi(0)\rangle$. Thus the evolving beam is

$$|\Psi(z)\rangle = \sum_{\sigma=\pm}\sum_{n=-\infty}^{\infty} c_n^\sigma e^{-i\mathcal{E}_n^\sigma z} |\mathcal{E}_n^\sigma\rangle. \tag{7}$$

We now project the evolving beam Eq. (7) to the Wannier-Bloch basis $|\sigma, q\rangle \equiv |\sigma\rangle \otimes |q\rangle$ where $|q\rangle = \frac{1}{\sqrt{2\pi}}\sum_{l=-\infty}^{\infty} |l\rangle\, e^{ilq}$ spans the quasi-momentum space:

$$\begin{aligned}\Psi_{\sigma,q}(z) \;\equiv\; (\sigma\,, q\,|\,\Psi(z)\rangle &= e^{-i\mathcal{E}_0^- z}\{C^-(\omega z + q)\,(\sigma\,, q|\,\mathcal{E}_0^-\rangle \\ &+\; e^{-i(\mathcal{E}_0^+ - \mathcal{E}_0^-)z} C^+(\omega z + q)\,(\sigma\,, q\,|\mathcal{E}_0^+\rangle\}\end{aligned} \tag{8}$$

where $(\sigma, q\,| \equiv (\sigma\,| \otimes \langle q\,|$, and $(\sigma\,| = (\mathcal{PT}|\,\sigma\rangle)^T$ [1]. The coefficients $C^\sigma(\omega z + q) \equiv \sum_{p=-\infty}^{\infty} c_p^\sigma e^{-ip(\omega z+q)}$ satisfy the periodicity relation $C^\sigma(\omega z + q + 2\pi) = C^\sigma(\omega z + q)$.

Equations (7,8) provide an explanation for the recombination and self-imaging events. They indicate that the evolving beam is, in general, not periodic as a function of the propagation distance z and it is characterized by two propagation scales: The first one is the Bloch period, $z_B = \frac{2\pi}{\omega}$, originating from the periodicity of the C^σ functions. The second scale $z_E = \frac{2\pi}{\mathcal{E}_0^+ - \mathcal{E}_0^-}$ is associated with the minimal energy spacing in-between the two Wannier-Stark ladders and arises from the nontrivial relative phase

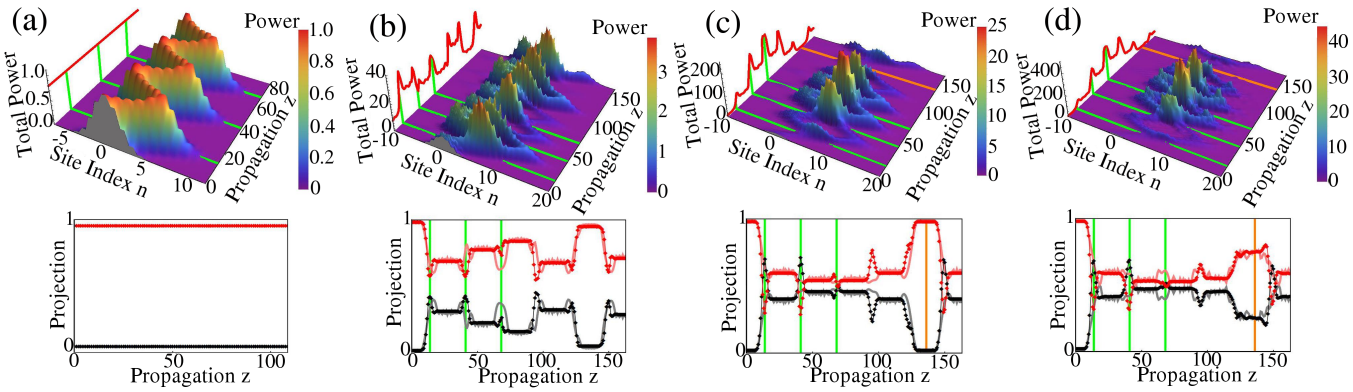

FIG. 3: (Color online) Propagation for an initial Gaussian wavefront $a_n(0) = b_n(0) = e^{-n^2/10}$. The lattice parameters are $\alpha = 1$, $\omega = 0.231$, and $A = 0.6$. The site index n indicates the n-th dimer where the amplifying site is juxtaposed with the attenuating site on the right. The red line (upper subfigures) shows the total power while the color map describe the individual site power $(|a_n(z)|^2, |b_n(z)|^2)$. The green lines mark the first three Zener distances z_Z while the orange lines mark the expected self-imaging time $z_{\rm SI}$. In the lower graphs the gray and pink lines correspond to the normalized relative band-power evaluated numerically from the beam evolution (see text). The black and red dots correspond to the upper and lower band-projections Eq. (9), normalized to the total power at each distant z. In (a) $\gamma = 0$, in (b) $\gamma = 0.405$, while in (c) and (d) $\gamma = 0.443$. In (d) a defect is included in the $7th$-dimer during the propagation interval $z \in [z_Z^{(1)} - 4, z_Z^{(1)} + 4]$ (see text for details). The presence of the defect disrupts the expected revival at $z_{\rm SI}$ (see the lower subfigure (c) where the expected $z_{\rm SI}$ is marked with an orange line) and results in a huge total power at the recombination distance z_R (third green line at upper subfigure d). The behaviour of subfigures b,c,d is typical and has been observed over a wide range of the parameter A.

on the rhs of Eq. (8). There are $\omega - \gamma$ values for which these two scales are rationally related to one another i.e. $z_E/z_B = N/M$. This condition leads to a self-imaging of the initial beam at distances $z_{SI} = Mz_E = Nz_B$. For instance, when $M = 1, N = 5$ the initial wavepacket is reconstructed at the distance $z_{SI} = \frac{10\pi}{\omega}$, (orange line in Fig. 3c. Moreover, a giant power focus (third green line) occurs at the recombination distance which is between two successive self-imaging events.

A deeper insight of the recombination events is achieved by evaluating the relative band projections $\tilde{P}^\sigma(z)$ of the evolving beam. Using Eq. (8) we get

$$\tilde{P}^\sigma(z) = \frac{P^\sigma(z)}{P^-(z) + P^+(z)}; P^\sigma(z) = \int |\Psi_{\sigma,q}(z)|^2 dq \quad (9)$$

The band projections are plotted on the lower row of Fig. 3 as black (upper) and red (lower) points. In the same figures the pink and grey lines correspond to the relative power (normalized $P^R(z) + P^L(z) = 1$) evaluated numerically as the power at the left and right sites of the recombination point, dimer index $n = 7$. The numerical results strongly correlate with the band projections Eq. (9) where the pink (left) and grey (right) lines correspond to the lower and upper bands respectively. The distances where jumps occur coincide with the position $z = z_Z^{(n)}$ where Zener inter-band transitions of power occurs according to the semi-classical picture of splittings and recombinations discussed earlier (see green lines).

We have also studied the effect of a defect in the creation of these intense recombination points. In general, a defect will devalue the maximum of the total power; however, a strategically placed defect at one of the recombination distances $z_Z^{(n)}$ can lead to further enhancement of the power peak. This is reported in Fig. 3d, where the real part of the refraction index of the $n = 7$ dimer, where the first recombination at distance $z = z_Z^{(1)} = \pi/\omega$ occurs (see Fig. 3c), has been altered i.e. $n\omega \to n\omega + 0.25$ (where $n = 7$). This alteration occurred during the propagation distance $\Delta z = z_Z^{(1)} \pm 4$ from the origin. We interpret this phenomenon as resulting from quasi-momentum randomization due to the scattering from the defect prior to the giant recombination. This leads to recombinations with all power concentrated in a narrow spatial domain.

In conclusion, we have investigated stable Bloch-Zener oscillations in a photonic lattice with local $\mathcal{PT}$-symmetry. We have found that an initial beam experiences a cascade of beam splittings and recombinations where the re-concentrated power can exceed the initial value due to the non-Hermitian nature of the dynamics. At the same time we have found that a judicial selection of the index gradient ω and the gain/loss parameter γ can result in perfect self-imaging of the initial packet at distances dictated by these two parameters. This platform can open up new possibilities for the realization of reconfigurable beam splitters, interferometers and imaging processing.

Acknowledgements - We acknowledge useful discussions with A. Szameit and R. El-Ganainy for the experimental implementation of our set-up. This work was partly sponsored by AFOSR MURI Grant No. FA9550-14-1-0037, and by NSF Grant No. DMR-1306984.

[1] C. M. Bender, S. Boettcher, Phys. Rev. Lett. **80**, 5243 (1998); C. M. Bender, Rep. Prog. Phys. **70**, 947 (2007).

[2] H. Cartarius, G. Wunner, Phys. Rev. A **86**, 013612 (2012); M. Kreibich, J. Main, H. Cartarius, G. Wunner, Phys. Rev. A **87**, 051601(R) (2013); M. Kreibich, J. Main, H. Cartarius, G. Wunner, Phys. Rev. A **90**, 033630 (2014); W. D. Heiss, H. Cartarius, G. Wunner, J. Main, J. Phys. A: Math. Theor. **46**, 275307 (2013).

[3] E-M Graefe, J. Phys. A: Math. Theor. **45**, 444015 (2012); M. Hiller, T. Kottos, A. Ossipov, Phys. Rev. A **73**, 063625 (2006)

[4] J. M. Lee, T. Kottos, B. Shapiro, Phys. Rev. B **91**, 094416 (2015).

[5] K. G. Makris *et al.*, Phys. Rev. Lett. **100**, 103904 (2008).

[6] C. E. Rüter *et al.*, Nat. Phys. **6**, 192 (2010); A. Guo, *et al.*, Phys. Rev. Lett. **103**, 093902 (2009).

[7] L. Feng *et al.*, Science **333**, 729 (2011).

[8] A. Regensburger, C. Bersch, M.A. Miri, G. Onishchukov, D. N. Christodoulides, U. Peschel, Nature **488**, 167 (2012).

[9] L. Chang *et al.*, Nat. Phot. **8**, 524 (2014).

[10] B. Peng *et al.*, Nat. Phys. **10**, 394 (2014).

[11] H. Hodaei *et al.*, Science **346**, 975 (2014); L. Feng *et al.*, Science **346**, 972 (2014).

[12] A. Mostafazadeh, Phys. Rev. Lett. **102**, 220402 (2009).

[13] S. Longhi, Phys. Rev. Lett. **103**, 123601 (2009).

[14] M. C. Zheng *et. al*, Phys. Rev. A **82**, 010103 (2010).

[15] H. Schomerus, Phys. Rev. Lett. **104**, 233601 (2010).

[16] A. A. Sukhorukov, Z. Xu, Y. S. Kivshar, Phys. Rev. A **82**, 043818 (2010).

[17] S. Longhi, Phys. Rev. A **82**, 031801 (2010); Y. D. Chong *et al.*, Phys. Rev. Lett. **106**, 093902 (2011).

[18] H. Ramezani, D. N. Christodoulides, V. Kovanis, I. Vitebskiy, T. Kottos, Phys. Rev. Lett. **109**, 033902 (2012); H. Ramezani, T. Kottos, V. Kovanis, D. N. Christodoulides, Phys. Rev. A **85**, 013818 (2012).

[19] J. Schindler *et al.*, J. Phys. A -Math and Theor. **45**, 444029 (2012); H. Ramezani *et al.*, Phys. Rev. A **85**, 062122 (2012); Z. Lin *et al.*, Phys. Rev. A **85**, 050101(R) (2012); N. Bender, S. Factor, J. D. Bodyfelt, H. Ramezani, D. N. Christodoulides, F. M. Ellis, T. Kottos, Phys. Rev. Lett. **110**, 234101 (2013)

[20] X. Zhu *et al.*, Phys. Rev. X **4**, 031042 (2014); R. Fleury, D. L. Sounas, and A. Alú, Nat. Comm. **6**, 5905 (2015).

[21] F. Dreisow, A. Szameit, M. Heinrich, T. Pertsch, S. Nolte, A. Tünnermann, S. Longhi, Phys. Rev. Lett. **102**, 076802 (2009)

[22] H. Trompeter, T. Pertsch, F. Lederer, D. Michaelis, U. Streppel, A. Bräuer, U. Peschel, Phys. Rev. Lett. **96**, 023901 (2006).

[23] H. Trompeter, W. Krolikowski, D. N. Neshev, A. S. Desyatnikov, A. A. Sukhorukov, Y. S. Kivshar, T. Pertsch, U. Peschel, F. Lederer, Phys. Rev. Lett. **96**, 053903 (2006).

[24] A. Szameit, T. Pertsch, S. Nolte, A. Tünnermann, U. Peschel, F. Lederer, J. Opt. Soc. Am. B **24**, 2632 (2007); A. Szameit, I. L. Garanovich, M. Heinrich, A. A. Sukhorukov, F. Dreisow, T. Pertsch, S. Nolte, A. Tünnermann, S. Longhi, Y. S. Kivshar, Phys. Rev. Lett. **104**, 223903 (2010).

[25] We consider the case where the distance between adjacent dimers is *slightly* larger than the distance between the two waveguides that compose the dimer and thus $\alpha > A/2$. We further point out that the distance between consequent a_n (b_n)-waveguides, i.e. a_n with $a_{n\pm1}$ (b_n with $b_{n\pm1}$) waveguides, is the largest distance between nearest neighbor waveguides and thus the associated coupling is smaller. In order to minimize the importance of this coupling we can: (i) design the cross section of the a_n and b_n waveguides in a way that it is not symmetric and thus the overlapping fields at the consequent a_n or b_n waveguides is minimal and (ii) include at the midpoint between adjacent a_n (b_n) waveguides a third passive defect waveguide c_n which is highly detuned with respect to the two other waveguides. Such defect waveguide will eliminate any coupling between consequent a_n (b_n) waveguides.

[26] O. Bendix, R. Fleischmann, T. Kottos, B. Shapiro, J. Phys. A: Math. Theor. **43** 265305 (2010).

[27] A. Mostafazadeh, Pramana-J. Phys. **73**, 269 (2009).

[28] With the term "asynchronous" we describe situations for which the period of the Zener tuneling and the BO period are not commensurate with one another.